Real-time management of faulty electrodes in electrical impedance tomography

Alzbeta E. Hartinger, Robert Guardo, Andy Adler, and Hervé Gagnon*

Abstract

Completely or partially disconnected electrodes are a fairly common occurrence in many EIT clinical applications. Several factors can contribute to electrode disconnection: patient movement, perspiration, manipulations by clinical staff and defective electrode leads or electronics. By corrupting several measurements, faulty electrodes introduce significant image artifacts. In order to properly manage faulty electrodes, it is necessary to 1) account for invalid data in image reconstruction algorithms and 2) automatically detect faulty electrodes. This paper presents a two-part approach for real-time management of faulty electrodes based on the principle of voltage-current reciprocity. The first part allows accounting for faulty electrodes in EIT image reconstruction without *a priori* knowledge of which electrodes are at fault. The method properly weights each measurement according to its compliance with the principle of voltage-current reciprocity. Results show that the algorithm is able to automatically determine the valid portion of the data and use it to calculate high quality images. The second part of the approach allows automatic real-time detection of at least one faulty electrode with 100% sensitivity and two faulty electrodes with 80% sensitivity enabling the clinical staff to fix the problem as soon as possible to minimize data loss.

Index Terms

Electrical impedance tomography, biomedical instrumentation, faulty electrodes, voltage-current reciprocity principle.

This work was supported in part by the Natural Sciences and Engineering Research Council of Canada and the Fonds québecois de la recherche sur la nature et les technologies. *Asterisk indicates corresponding author.*

*H. Gagnon is with the Institut de génie biomédical, École Polytechnique de Montréal, Montréal, QC H3C 3A7, Canada (e-mail: gagnon@igb.polymtl.ca).

A.E. Hartinger and R. Guardo are with the Institut de génie biomédical, École Polytechnique de Montréal, Montréal, QC H3C 3A7, Canada (e-mail: guardo@igb.polymtl.ca).

A. Adler is with the Department of Systems and Computer Engineering, Carleton University, Ottawa, ON K1S 5B6, Canada.

Real-time management of faulty electrodes in electrical impedance tomography

I. Introduction

ELECTRICAL impedance tomography (EIT) is a biomedical technique for imaging the electrical conductivity distribution of a body section. EIT systems generally use 16 or more body surface electrodes to measure voltages produced while applying low amplitude sinusoidal currents. These voltage measurements are then converted to conductivity images by solving a regularized inverse model typically formulated on a finite element mesh.

Completely or partially disconnected electrodes are a fairly common occurrence in many EIT clinical applications. While completely detached electrodes correspond to infinite contact impedance, partial disconnections are associated with electrodes which are physically attached but with high contact impedance. Many factors can contribute to electrode disconnection: patient movement, perspiration, manipulations by clinical staff and defective electrode leads or electronics. By corrupting several measurements, faulty electrodes introduce significant image artifacts. In all EIT applications, proper management of faulty electrodes is therefore mandatory and should include 1) accounting for invalid data in image reconstruction algorithms and 2) faulty electrode detection.

In long-term cardiopulmonary monitoring at the bedside [1], [2], electrode faults should be signaled to the clinical staff as soon as possible to minimize data loss. However, a rare condition could have occurred while electrodes were still at fault requiring coherent image reconstruction from the partially corrupted data. For epileptogenic zone localization [3], [4], patients are monitored for extended periods awaiting seizures during which the probability of electrodes becoming partially detached momentarily is fairly high. Since electrode disconnections cannot be fixed during data acquisition, reconstruction algorithms must properly account for partially invalid data. Some applications, such as skin cancer detection [5], require an electrode matrix mounted at the tip of a hand-held measurement probe. While a large portion of the electrodes will interface properly with the skin, others will have high contact impedance. This could result from an unusual three dimensional lesion morphology, localized skin

hyperkeratosis or a misfit of the electrode array to the investigated body part which would prevent some electrodes from properly touching the skin.

So far, two methods have been described in the literature for managing faulty electrodes. Adler [6] modified the measurement noise covariance matrix in the maximum *a posteriori* (MAP) reconstruction algorithm to compensate for invalid data from disconnected electrodes. However, the method is not applicable by itself in clinical practice since it requires *a priori* knowledge of the faulty electrodes. For this purpose, Asfaw and Adler [7] proposed an algorithm for automatic detection of one erroneous electrode. Images are reconstructed by the previous algorithm while supposing each electrode successively disconnected. These image reconstructions are then used to estimate the supposed invalid data which is compared to the actual measurements to confirm or infirm the faulty electrode hypothesis. Although reliable for its intended purpose, the method cannot properly handle multiple disconnections. Furthermore, it is not applicable in real time since it requires an extensive number of calculations.

To circumvent these problems, this paper presents a complete real-time management method for partially and completely disconnected electrodes. The proposed approach is based on the principle of voltage-current reciprocity and includes 1) accounting for invalid data in image reconstruction algorithms and 2) faulty electrode detection.

II. Principle of voltage-current reciprocity

The principle of voltage-current reciprocity states that data acquired with an excitation and measurement pair of electrodes is equivalent, under ideal conditions, to data obtained by inverting the electrode pairs [8]. Fig. 1 illustrates the *adjacent-drive adjacent-measurement* protocol implemented in our system [9] where current flow is indicated by arrows and the measurement pair by a voltmeter. Since our system uses $N = 16$ body surface electrodes, $N(N-3) = 208$ measurements are acquired among which only half are independent due to the principle of voltage-current reciprocity. One example of reciprocal measurements is outlined in Fig. 1 by continuous (—) circles (measurements 1 and 195) while another is outlined by dash-dotted (-··-) circles (measurements 16 and 194).

In the case of faulty electrodes, the affected measurements will obviously not respect the voltage-current reciprocity principle. When the erroneous electrode is part of the excitation pair, no current will flow through the faulty electrode while some current may be applied by the properly connected electrode if the current sources are designed as single-ended. When the faulty electrode is part of the measurement pair, inconsistent data will be

acquired since one input of the differential amplifier is floating. In all of the above instances, the voltage-current reciprocity principle will not be respected. This characteristic will be used later to pinpoint erroneous measurements in the proposed two-step faulty electrode management method.

III. Accounting for invalid data in image reconstruction algorithms

In order to automatically account for invalid data, we propose an extension of the maximum *a posteriori* (MAP) approach of Adler [6]. The MAP algorithm requires a linearized formulation of the forward problem which is obtained by solving Maxwell's equations using the finite element method (FEM) [10]. The FEM model typically consists of a triangular or tetrahedral mesh representation of the medium where conductivity is supposed constant inside each element and a piecewise linear interpolation is used to approximate the voltage distribution inside the medium. Such a FEM model will result in the following matrix formulation of the forward problem:

$$\boldsymbol{V} = \boldsymbol{f}(\boldsymbol{\sigma}) = \boldsymbol{Y}^{-1}\boldsymbol{I}, \tag{1}$$

where $\boldsymbol{V}$ represents the surface voltage measurement vector, $\boldsymbol{\sigma}$, the conductivity distribution vector, $\boldsymbol{I}$, the current intensity vector and $\boldsymbol{Y}$ is the medium admittance matrix which depends on $\boldsymbol{\sigma}$.

The preceding equation is linearized around a reference conductivity distribution vector $\boldsymbol{\sigma}_0$ using a Taylor series expansion:

$$\underbrace{(\boldsymbol{V} - \boldsymbol{V}_0)}_{\boldsymbol{z}} = \underbrace{\left.\frac{\partial \boldsymbol{f}(\boldsymbol{\sigma})}{\partial \boldsymbol{\sigma}}\right|_{\boldsymbol{\sigma}=\boldsymbol{\sigma}_0}}_{\boldsymbol{H}} \underbrace{(\boldsymbol{\sigma} - \boldsymbol{\sigma}_0)}_{\boldsymbol{x}}, \tag{2}$$

which is equivalent to the following matrix relation:

$$\boldsymbol{z} = \boldsymbol{H}\boldsymbol{x} + \boldsymbol{n}, \tag{3}$$

where $\boldsymbol{z}$ is the voltage measurement change vector, $\boldsymbol{H}$, the linear operator relating measurements to conductivity, $\boldsymbol{x}$, the conductivity change vector, and $\boldsymbol{n}$, the measurement noise vector.

The MAP solution is the most probable conductivity change vector $\boldsymbol{x}$ given the observed voltage measurement

change vector $\boldsymbol{z}$ [11] which corresponds to maximizing the probability density function of $\boldsymbol{x}$ given $\boldsymbol{z}$:

$$\hat{\boldsymbol{x}}_{\mathrm{MAP}} = \arg\max_{\boldsymbol{x}}[f(\boldsymbol{x}|\boldsymbol{z})]. \tag{4}$$

By applying Bayes' formula knowing that $f(\boldsymbol{z})$ is independent of $\boldsymbol{x}$, this relation becomes:

$$\hat{\boldsymbol{x}}_{\mathrm{MAP}} = \arg\max_{\boldsymbol{x}}\left(\frac{f(\boldsymbol{z}|\,\boldsymbol{x})f(\boldsymbol{x})}{f(\boldsymbol{z})}\right) = \arg\max_{\boldsymbol{x}}\left[f(\,\boldsymbol{z}|\,\boldsymbol{x})f(\boldsymbol{x})\right]. \tag{5}$$

To characterize $f(\,\boldsymbol{z}|\,\boldsymbol{x})$ and $f(\boldsymbol{x})$, the following probabilistic hypotheses are used: $\boldsymbol{x} \sim N(\boldsymbol{0}, \boldsymbol{R}_x)$ and $\boldsymbol{n} \sim N(\boldsymbol{0}, \boldsymbol{R}_n)$, where $N(\boldsymbol{\mu}, \boldsymbol{\Gamma})$ represents a multidimensional Gaussian distribution with $\boldsymbol{\mu}$ average and $\boldsymbol{\Gamma}$ covariance matrix.

By combining these hypotheses with (5), the final MAP estimate can be obtained [12]:

$$\hat{\boldsymbol{x}}_{\mathrm{MAP}} = \left(\boldsymbol{H}^{\mathrm{T}}\boldsymbol{R}_n^{-1}\boldsymbol{H} + \lambda\boldsymbol{R}_x^{-1}\right)^{-1}\boldsymbol{H}^{\mathrm{T}}\boldsymbol{R}_n^{-1}\boldsymbol{z} \tag{6}$$

$$= \boldsymbol{B}\left(\boldsymbol{R}_n^{-1}, \boldsymbol{R}_x^{-1}, \lambda\right)\boldsymbol{z}, \tag{7}$$

where λ controls the relative weighting of the $\hat{\boldsymbol{x}}_{\mathrm{MAP}}$ mismatch against the *a priori* information and the observed measurements. Among all methods available to adjust λ, we selected the fixed noise figure method whose merit has been demonstrated by Graham and Adler [13]. $\boldsymbol{R}_x^{-1}$ is set to $\boldsymbol{F}^T\boldsymbol{F}$ where the matrix $\boldsymbol{F}$ is a high-pass filter used to amplify the undesired $\boldsymbol{x}$ vector components that will be eliminated by the minimization process of the MAP algorithm. This approach penalizes reconstructed images with an unsmooth conductivity distribution [11]. Since noise is independent for each measurement, $\boldsymbol{R}_n^{-1}$ can be represented as a diagonal matrix whose diagonal term $\boldsymbol{R}_n^{-1}(k,k)$ corresponds to $1/\boldsymbol{\sigma}_{n,k}^2$ which represents the inverse of the k^{th} measurement variance.

A. Methods for selecting $\boldsymbol{\sigma}_{n,k}^2$

In this paper, three methods for selecting $\boldsymbol{\sigma}_{n,k}^2$ will be compared in section V. *Method 1* is the regular MAP algorithm which does not account for faulty electrodes [11]. Since, in normal conditions, the noise distribution is considered homogeneous for each measurement, $\boldsymbol{\sigma}_{n,k}^2$ is set to a constant value for every k. This is equivalent to replacing $\boldsymbol{R}_n^{-1}$ by an identity matrix and incorporating the constant value for $\boldsymbol{\sigma}_{n,k}^2$ inside the λ factor in (6).

Method 2 is the method proposed by Adler [6] to account for faulty electrodes. When an electrode is partially or completely disconnected, every measurement performed using this electrode, either to apply current or measure voltage, will be suspicious and should not be taken into account during the image reconstruction process. The faulty electrodes have to be identified first, either by an operator or an automatic algorithm [7]. Every measurement performed using one or more of the faulty electrodes is then identified as suspicious. For every suspicious measurement, $\boldsymbol{\sigma}_{n,k}^2 \rightarrow \infty$ which is equivalent to setting $\boldsymbol{R}_n^{-1}(k,k)$ to zero and corresponds to a measurement whose variance is so great that the algorithm should not take it into account at all. For all other measurements, $\boldsymbol{\sigma}_{n,k}^2$ is set to a constant value as in *method 1*. This method is easy to apply and works well but assumes that the faulty electrodes are known or can be easily identified automatically which is rarely the case in clinical practice. Furthermore, this method applies an all or nothing approach where measurements are categorized in only two groups. Measurements performed with partially disconnected electrodes, whose contact impedance is simply higher than normal, must be arbitrarily treated either as suspicious or normal.

To circumvent these problems, we propose *method 3* which can adjust $\boldsymbol{\sigma}_{n,k}^2$ for partially or completely disconnected electrodes without *a priori* knowledge of the faulty electrodes. The first step of the method consists in comparing reciprocal EIT data vectors to identify erroneous measurements that do not comply with the principle of voltage-current reciprocity.

We define a reciprocal vector, $\boldsymbol{V}_{\mathrm{R}}$, where every measurement of the EIT data signal $\boldsymbol{V}$ is replaced by the reciprocal measurement obtained by inverting the excitation and measurement pair of electrodes. Both $\boldsymbol{V}$ and $\boldsymbol{V}_{\mathrm{R}}$ are normalized by their maximum value and are therefore unitless. A quadratic reciprocity error vector, $\boldsymbol{e}^2$, is then computed between $\boldsymbol{V}$ and $\boldsymbol{V}_{\mathrm{R}}$:

$$\boldsymbol{e}^2 = (\boldsymbol{V} - \boldsymbol{V}_{\mathrm{R}})^2. \tag{8}$$

Fig. 2(a) presents an EIT data signal $\boldsymbol{V}$ acquired with our system on a resistor mesh phantom with four disconnected electrodes. Figures (b) and (c) respectively show the corresponding reciprocal EIT signal $\boldsymbol{V}_{\mathrm{R}}$ and the quadratic reciprocity error vector $\boldsymbol{e}^2$. Fig. 3 presents the same results as Fig. 2(c) but for four partially disconnected electrodes that were created by connecting 10 kΩ resistors in series with the electrode leads. Fig. 2(c) and Fig. 3 show that the maximum quadratic reciprocity error is 0.19 for partially disconnected electrodes and reaches 0.98 for

completely disconnected electrodes. Quadratic reciprocity error therefore reflects the precision of each measurement and can be used to adjust $\boldsymbol{\sigma}_{n,k}^2$. A large quadratic error $\boldsymbol{e}_k^2$ should correspond to a large $\boldsymbol{\sigma}_{n,k}^2$ and *vice versa*. To provide a smooth transition, we elected to use the following simple relation:

$$\boldsymbol{\sigma}_{n,k}^2 = \exp\left(\frac{\boldsymbol{e}_k^2}{\tau}\right), \tag{9}$$

where τ is a unitless constant determined experimentally. The above relation is illustrated in Fig. 4 by a dashed line for $\tau = 2.5 \times 10^{-7}$. *Method 2* can also be formulated as a step function which is represented by a solid line. Close inspection shows that both methods are equivalent for extreme $\boldsymbol{e}_k^2$ values. Each diagonal element $\boldsymbol{R}_n^{-1}(k,k) = 1/\boldsymbol{\sigma}_{n,k}^2$ is computed from the above exponential equation which results in automatic management of both partially or completely disconnected electrodes.

The following algorithm summarizes the three methods:

m = number of measurements
$\boldsymbol{R}_x^{-1} = \boldsymbol{F}^T\boldsymbol{F}$ % where $\boldsymbol{F}$ is a high-pass filter
$\boldsymbol{R}_n^{-1} = \mathbf{0}_m$ % where $\mathbf{0}_m$ is a zero-filled matrix

for k = 1 to m
  if Method == 1
    $\boldsymbol{R}_n^{-1}(k,k)$ = 1
  else if Method == 2
    if measurement is suspicious
      $\boldsymbol{R}_n^{-1}(k,k)$ = 0
    else
      $\boldsymbol{R}_n^{-1}(k,k)$ = 1
  else if Method == 3
    $\boldsymbol{R}_n^{-1}(k,k) = \exp\left(-\frac{\boldsymbol{e}_k^2}{\tau}\right)$

$\boldsymbol{B} = \boldsymbol{B}\left(\boldsymbol{R}_n^{-1}, \boldsymbol{R}_x^{-1}, \lambda\right)$

IV. Real-time detection of faulty electrodes

The proposed algorithm for real-time detection of poorly attached or completely disconnected electrodes is based on the principle of voltage-current reciprocity in a similar manner as *method 3* from the previous section. The algorithm starts by computing the quadratic reciprocity error vector $\boldsymbol{e}^2$ between $\boldsymbol{V}$ and $\boldsymbol{V}_{\mathrm{R}}$ using (8). The next step consists in computing a matrix, $\mathbf{AffectMeas}$, which associates each electrode with the measurements in which it is involved.

```
n = number of electrodes
m = number of measurements

for i = 1 to n
   for k = 1 to m
      if k^th measurement involves i^th electrode
         AffectMeas(k,i) = 1
      else
         AffectMeas(k,i) = 0
```

A vector representing the total quadratic error for every electrode, $\mathbf{TQE}$, is then computed and normalized, $\mathbf{TQEn}$:

```
for i = 1 to n
   TQE(i) = 0
   for k = 1 to m
      TQE(i) = TQE(i) + AffectMeas(k,i) * e^2(k)

for i = 1 to n
   TQEn(i) = TQE(i)/max(TQE) * 100
```

Fig. 5(a) presents an EIT data signal $\boldsymbol{V}$ acquired with our system on a resistor mesh phantom when no electrode is disconnected. Figures (b) and (c) respectively show the corresponding quadratic reciprocity error vector $\boldsymbol{e}^2$ and normalized total quadratic error $\mathbf{TQEn}$. Fig. 6(a) presents the same results as Fig. 5(c) but with one faulty electrode. All scenarios where two electrodes are erroneous can be summarized by two typical cases: two non-adjacent Fig. 6(b) and two adjacent (c) faulty electrodes.

When no electrode is faulty, the quadratic reciprocity error for all measurements is small (Fig. 5(b)). This results in similar **TQE** values for all electrodes which explains why **TQEn** values (c) are all close to 100%. A first faulty electrode can be identified (Fig. 6(a)) when the minimum **TQEn** value is below a specific threshold. The optimal value for this threshold was determined experimentally to be around 20% by analyzing results where at least one electrode was erroneous. The first faulty electrode is associated with the maximum **TQEn** value. A second erroneous electrode is identified (Fig. 6(b)) when the second highest **TQEn** value exceeds 95%. The specific value for this threshold was also obtained experimentally by analyzing results where two electrodes were erroneous. The second faulty electrode corresponds to the second maximal **TQEn** value. The following algorithm summarizes the detection method:

```
if minimal TQEn < 20
   electrode with maximal TQEn is faulty
   if second maximal TQEn > 95
      electrode with second maximal TQEn is also faulty
```

This algorithm is suitable, as is, to most EIT measurement processes where the principle of voltage-current reciprocity may be applied. However, in the *adjacent-drive adjacent-measurement* protocol, an additional scenario must be considered: two adjacent faulty electrodes. In this case, experimental results have shown that the **TQEn** values of four adjacent electrodes exceed 95%. While one may assume that four adjacent electrodes are faulty, only the two middle electrodes are erroneous even if their **TQEn** values are not the highest among the four adjacent electrodes. Fig. 6(c) illustrates an example where two adjacent electrodes (4 and 5) are faulty. The **TQEn** values corresponding to electrodes 3 and 6 are also above 95% since they perform many measurements in association with a faulty adjacent electrode.

V. Results

In order to test the efficiency of the proposed management method, measurements were acquired with our EIT system on a resistor mesh phantom and on a healthy male subject. A detailed description of our EIT system is presented in [9]. The phantom represents a circular homogeneous medium and is composed of 340 0.1% precision resistors (17 different nominal values ranging from 51.1 to 3160 Ω) [14]. By shunting one or several of the resistors,

localized perturbations can be produced. Since electrode leads are attached to the phantom by snap connectors, they can be individually detached to simulate complete disconnections. To simulate a partial electrode disconnection, a resistor is connected in series with the snap connector. This series resistor is negligible compared to the high input impedance of our voltage preamplifier and high output impedance of our current source. EIT data are therefore unaffected until the resistor value is greater than 5 kΩ where saturation of the current source occurs because of its limited compliance. This non-linearity will affect the reciprocity of the measurements. In this paper, 10 kΩ resistors were therefore selected to simulate partial disconnections.

EIT data were acquired with all electrodes properly connected and for different scenarios of partially and/or completely disconnected electrodes. Acquisitions were performed for 102 scenarios of up to four completely and/or partially disconnected electrodes and for five different measurement protocols: *adjacent-drive adjacent-measurement* (Fig. 1(a)), *opposite-drive adjacent-measurement* (Fig. 7(a)), *pseudo-opposite-drive adjacent-measurement* (c), *adjacent-drive opposite-measurement* (b), and *adjacent-drive pseudo-opposite-measurement* (d). The first protocol is commonly used by many EIT systems and conveniently provides all reciprocal measurement pairs. The two following protocols are documented in the literature [15] but do not perform reciprocal measurements. The *adjacent-drive opposite-measurement* and *adjacent-drive pseudo-opposite-measurement* protocols respectively provide reciprocal data for the *opposite-drive adjacent-measurement* and *pseudo-opposite-drive adjacent-measurement* protocols. Applying our faulty electrode management method therefore requires concatenation of data acquired from two reciprocal protocols if the measurement protocol does not already provide all reciprocal measurement pairs. The only penalty incurred is a reduction of the frame rate by half.

A. Faulty data management in reconstruction algorithms

Time difference images were reconstructed for all of the above scenarios to compare the three methods described in section III. Fig. 8 shows four representative cases corresponding to data acquired on the mesh phantom where four conductive targets were created by shunting specific resistors of the mesh. Since time difference images represent conductivity changes between two instants, data acquired on the homogeneous mesh phantom without any disconnected electrode were used as reference for all images. Column A shows a basic scenario where one electrode is completely disconnected. B and C illustrate more complex scenarios where two electrodes are completely

and partially disconnected by inserting 10 kΩ resistors. D presents an extreme scenario where four electrodes are partially disconnected. The partial or complete disconnection of a specific electrode is illustrated by a 10 kΩ or infinite resistor respectively. Time difference images from each line were reconstructed with *method 1, 2 or 3* as described in section 3. *Method 1*, which does not account for faulty electrodes, has been used for comparison purposes to reconstruct images from data acquired with no disconnected electrode (*method 1a*) and with faulty electrodes in compliance with the scenario of each column (*method 1b*). Since *method 2* requires *a priori* knowledge of the faulty electrodes, *method 2a* corresponds to the realistic electrode detection approach presented in [7], which only detects one faulty electrode, while *method 2b* presents a hypothetical scenario where all faulty electrodes would be formerly known.

In order to quantitatively compare the methods, a quadratic error ϵ^2, presented under each subfigure, was computed between all images and the corresponding first-line reference image using the following definition:

$$\epsilon^2 = (\boldsymbol{\sigma} - \boldsymbol{\sigma}_{\mathrm{R}})^{\mathrm{T}}(\boldsymbol{\sigma} - \boldsymbol{\sigma}_{\mathrm{R}}), \tag{10}$$

where $\boldsymbol{\sigma}$ is the conductivity distribution vector of each image compared to the *reference* vector $\boldsymbol{\sigma}_{\mathrm{R}}$.

Data acquired on a healthy male subject was used to reconstruct time difference images showing conductivity variations between full inspiration and expiration (Fig. 9). The layout of the figure is the same as Fig. 8 except for quadratic errors which were omitted. Since full inspiration and expiration are not reproducible references, such errors would not provide reliable quantitative comparisons.

In Fig. 8, first-line reference images accurately show the four expected conductive targets. Since *method 1* does not account for faulty electrodes, second-line images contain large artifacts associated with large quadratic errors. *Method 2a* uses the detection approach presented in [7] which cannot detect more than one faulty electrode. Therefore, only the first image of the third line is properly reconstructed. *Method 2b* and *3* reconstruct adequate images for all scenarios. However, close inspection shows that *method 3* reproduces the four conductive targets with higher resolution especially for scenarios B and D. This observation is confirmed by the lower quadratic error values except for scenario A. This anomaly results from the fact that we use the same τ value which was optimized to provide good image reconstructions overall. If τ had been optimized for scenario A, we would have obtained a

quadratic error of 4.76 which is smaller than that of *method 2*.

In Fig. 9, first-line images properly show two non-conductive elliptic regions associated with the lungs. As in Fig. 8, second-line images contain large artifacts because *method 1* does not account for faulty electrodes. Since *method 2a* uses an algorithm which cannot detect more than one faulty electrode, only the first image of the third line is properly reconstructed. *Method 2b* and *3* reconstruct adequate images for all scenarios. However, one has to remember that only *method 3* is applicable in practice since it requires no *a priori* knowledge of the faulty electrodes.

B. Automatic faulty electrode detection algorithm

EIT data from all scenarios were tested with our automatic faulty electrode detection algorithm and results are summarized in Table I. Results are classified by measurement protocol and number of faulty electrodes. For each measurement protocol, results are presented in two columns. The first column gives the number of data sets acquired with this measurement protocol for scenarios where a given number of electrodes are faulty. The second column indicates the number of electrodes correctly detected as faulty with the corresponding percentage of data sets which produced this result.

Table I shows that the algorithm performs with very high sensitivity up to two faulty electrodes. When three electrodes are erroneous, the algorithm always detects at least one faulty electrode. In 31% of cases, two faulty electrodes were correctly identified. In one scenario, where three consecutive electrodes were faulty, the algorithm appropriately printed a message stating that three adjacent electrodes had a **TQEn** value higher than 95%. When four electrodes are erroneous, the algorithm only detected one faulty electrode in 30% of cases. This results from too many erroneous measurements which makes it difficult for the algorithm to detect faulty electrodes using the principle of voltage-current reciprocity.

VI. Discussion and conclusion

This paper described a two-part approach for managing faulty electrodes in real time based on the principle of voltage-current reciprocity. The first part allowed accounting for faulty electrodes in EIT image reconstruction without *a priori* knowledge of which electrodes are at fault. The method properly weights every measurement

according to its compliance with the principle of voltage-current reciprocity instead of rejecting a whole set of measurements performed with a faulty electrode. Results showed that the algorithm was able to adequately exploit the valid portion of the data. In some cases, *method 2b* performed as well as the proposed method. However, one has to remember that *method 2b* cannot be applied automatically in practice since it requires *a priori* knowledge of all faulty electrodes. Furthermore, when the disconnection is momentary and only affects a few measurements of a data set, the proposed method would only reject these measurements while *method 2* would either overlook the situation or reject all measurements performed with the faulty electrode.

When less than four electrodes were disconnected, the second part of the approach allowed automatic real-time detection of at least one faulty electrode with 100% sensitivity and two faulty electrodes with 80% sensitivity. This would enable the clinical staff to fix the problem as soon as possible to minimize data loss. Once the identified electrodes are reconnected, remaining faulty electrodes would then be readily detected by the real-time algorithm. In the unlikely event where more than three electrodes are disconnected, the sensitivity is low since too many measurements are affected. This is not a major issue since in practice the disconnections would most likely occur sequentially and the real-time algorithm would promptly detect them as they become faulty. Parameters of the algorithm could be adapted to detect more faulty electrodes but with much reduced sensitivity since too many measurements are then affected.

The method is suitable to all data acquisition protocols involving four-electrode measurements for which the principle of voltage-current reciprocity is applicable. However, the protocol should provide all reciprocal measurement pairs. If not, acquisition must also be performed with the reciprocal acquisition protocol as described in section V. This would require modifying an EIT system to alternatively acquire data from reciprocal protocols which results in reducing the frame rate by half. The method has been demonstrated with the MAP algorithm but is also suitable to other reconstruction algorithms as described by Adler [6]. Other systems and algorithms may require adjusting τ.

For clinical applications of EIT, faulty electrodes are a major issue requiring proper management. Given the simplicity of the approach and the quality of the results, the proposed method would be a worthy addition to most EIT systems. Some systems include specialized hardware to automatically detect faulty electrodes. Although such hardware could warn the clinical staff that some electrodes are faulty, there are situations where this is clearly

insufficient. For instance, during an epileptic seizure, coherent images have to be reconstructed since the partially corrupted data cannot be simply reacquired. Therefore, the proposed approach would also be a worthy addition to such systems.

REFERENCES

[1] I. Frerichs, "Electrical impedance tomography (EIT) in applications related to lung and ventilation: a review of experimental and clinical activities," *Physiol. Meas.*, vol. 21, no. 2 pp. R1-R21, May 2000.

[2] N. Coulombe, H. Gagnon, F. Marquis, Y. Skrobik and R. Guardo "A parametric model of the relationship between EIT and total lung volume," *Physiol. Meas.*, vol. 26, no. 4, pp. 401–411, Aug. 2005.

[3] D. S. Holder, *Electrical Impedance Tomography Methods, History and Applications*. Bristol, U.K.: Inst. Phys. Pub., 2005.

[4] L. Fabrizi, M. Sparkes, L. Horesh, J.F. Perez-Juste Abascal, A. McEwan, R.H. Bayford, R. Elwes, C.D. Binnie and D.S. Holder "Factors limiting the application of electrical impedance tomography for identification of regional conductivity changes using scalp electrodes during epileptic seizures in humans," *Physiol. Meas.*, vol. 27, no. 5, pp. S163–S174, May 2006.

[5] D. Narayanaswamy, "Feasibility study of instruments for electrical impedance tomography (EIT) and magentic [sic] induction measurement of skin cancer," M.S. thesis, Dept. Comput. Eng., Univ. Missouri-Rolla, Rolla, MO, 2006.

[6] A. Adler, "Accounting for erroneous electrode data in electrical impedance tomography," *Physiol. Meas.*, vol. 25, no. 1, pp. 227–238, Feb. 2004.

[7] Y. Asfaw and A. Adler, "Automatic detection of detached and erroneous electrodes in electrical impedance tomography," *Physiol. Meas.*, vol. 26, no. 2, pp. S175–S183, Apr. 2005.

[8] D. B. Geselowitz, "An application of electrocardiographic lead theory to impedance plethysmography," *IEEE Trans. Biomed. Eng.*, vol. 18, no. 1, pp. 38–41, Jan. 1971.

[9] A. E. Hartinger, H. Gagnon, and R. Guardo, "A method for modelling and optimizing an electrical impedance tomography system," *Physiol. Meas.*, vol. 27, no. 5, pp. S51–S64, May 2006.

[10] J. N. Reddy *An Introduction to the Finite Element Method*. New York, USA: McGraw-Hill, 1993.

[11] A. Adler and R. Guardo, "Electrical impedance tomography: regularized imaging and contrast detection," *IEEE Trans. Med. Imag.*, vol. 15, no. 2, pp. 170–179, Apr. 1996.

[12] A. E. Hartinger, H. Gagnon, and R. Guardo, "Accounting for hardware imperfections in EIT image reconstruction algorithms," *Physiol. Meas.*, vol. 28, no. 7, pp. S13–S27, Jul. 2007.

[13] B. M. Graham and A. Adler, "Objective selection of hyperparameter for EIT," *Physiol. Meas.*, vol. 27, no. 5, pp. S65–S79, May 2006.

[14] H. Gagnon and R. Guardo, "A method for designing electrical impedance tomography (EIT) phantoms of arbitrary shape and conductivity distribution," *Biomed. Tech.*, vol. 50, suppl. 1, pp. 297-298, 2005.

[15] X. Shi, X. Dong, W. Shuai, F. You, F. Fu, and R. Liu, “Pseudo-polar drive patterns for brain electrical impedance tomography,” *Physiol. Meas.*, vol. 27, no. 11, pp. 1071-1080, Nov. 2006.

LIST OF FIGURES

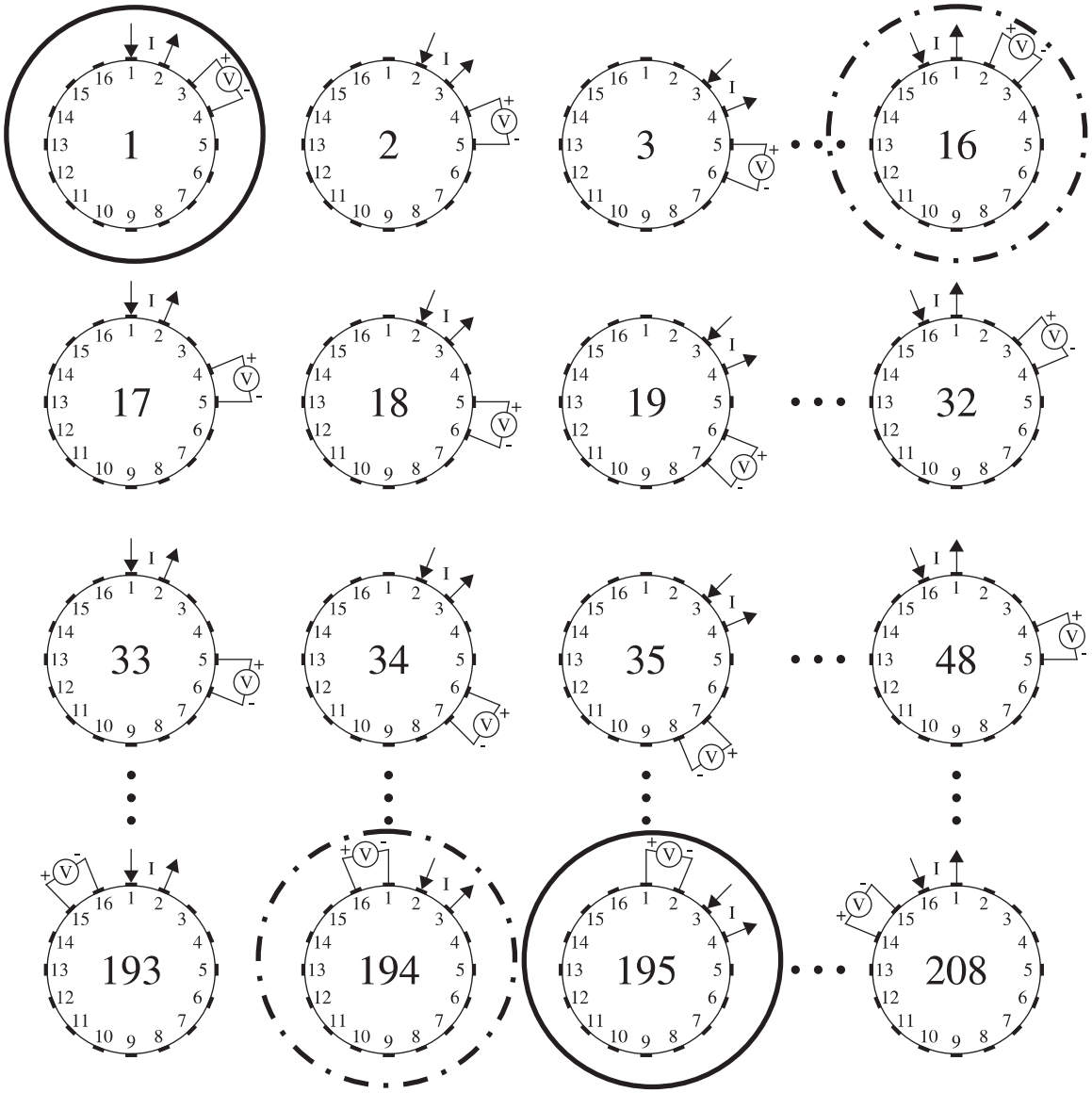

Fig. 1. Measurement sequence used in our system. One example of reciprocal measurements is outlined by (—) circles while another is highlighted by (-··-).

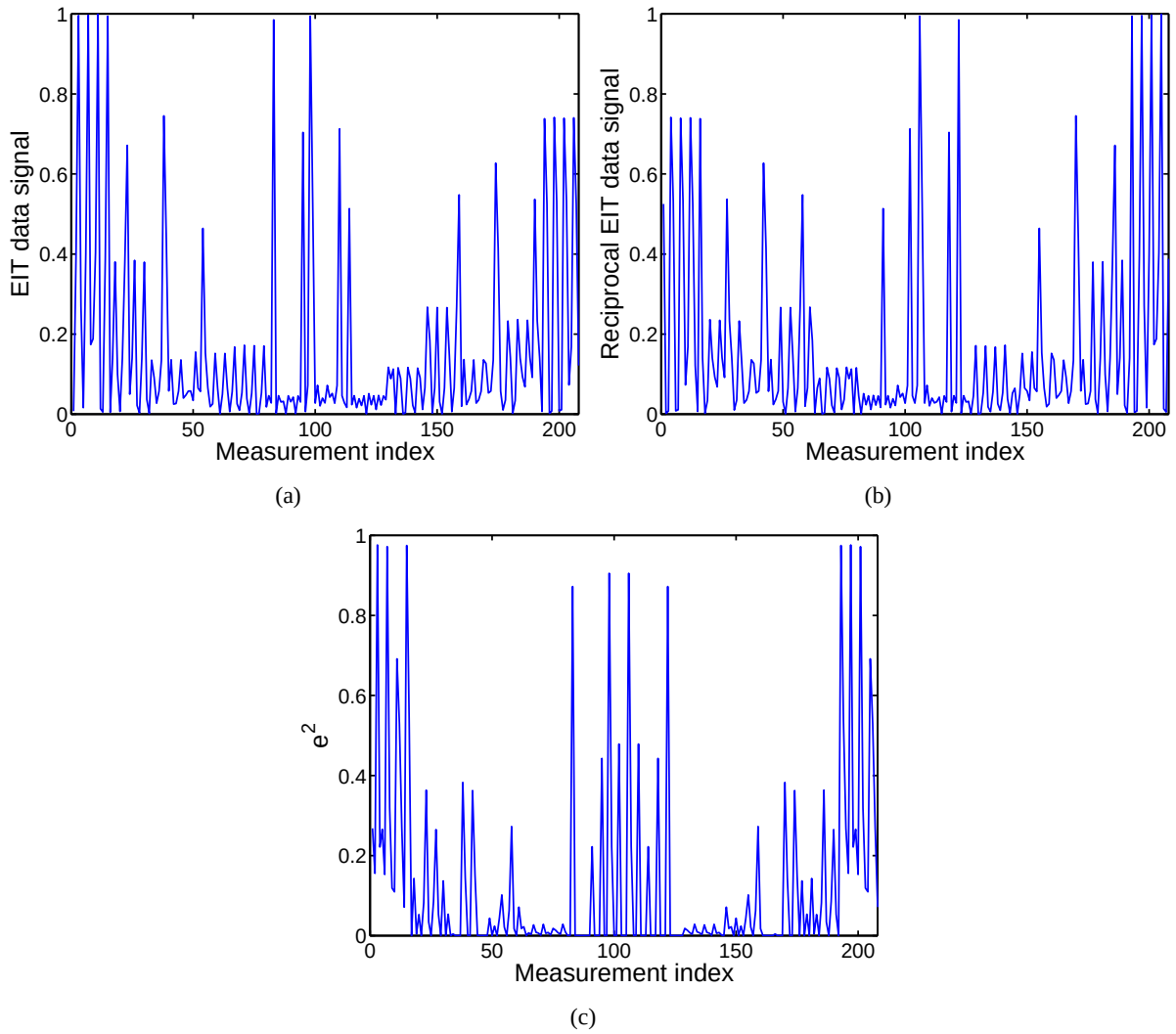

Fig. 2. Computing process of the quadratic reciprocity error vector. (a) EIT data signal acquired on a circular resistor mesh phantom with electrodes 3, 7, 11 and 15 completely disconnected. (b) Corresponding reciprocal EIT signal. (c) Quadratic reciprocity error vector. EIT data were acquired using the measurement sequence illustrated in Fig. 1.

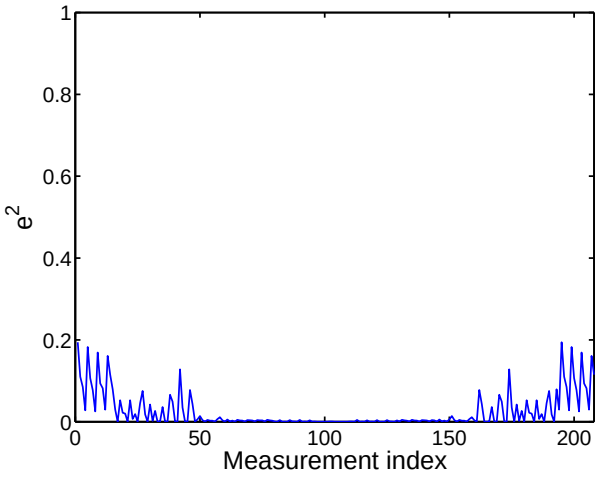

Fig. 3. Quadratic reciprocity error vector for four partially disconnected electrodes (3, 7, 11 and 15).

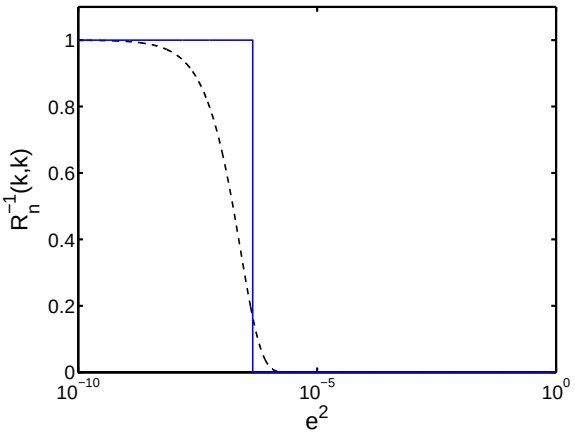

Fig. 4. Exponential function $\exp(-\boldsymbol{e}_k^2/\tau)$ (dashed line) used to modify the diagonal elements $\boldsymbol{R}_n^{-1}(k,k)$. Factor τ was determined experimentally and is equal to $2.5\text{x}10^{-7}$.

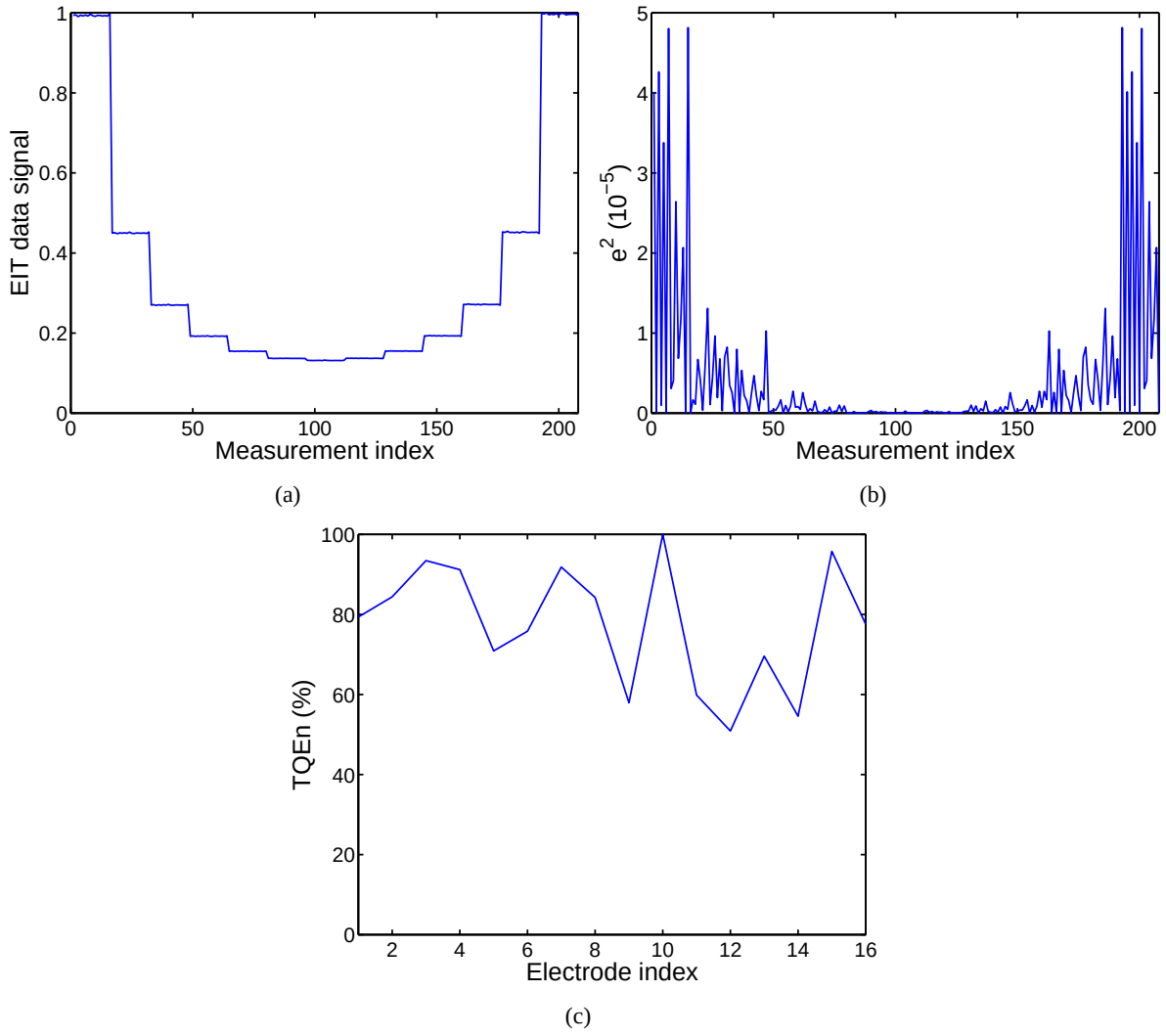

Fig. 5. Illustration of the detection process when no electrode is disconnected. (a) Voltage measurement signal acquired on a circular resistor mesh phantom. (b) Corresponding quadratic reciprocity error vector. (c) Normalized total quadratic error (**TQEn**) in percentage.

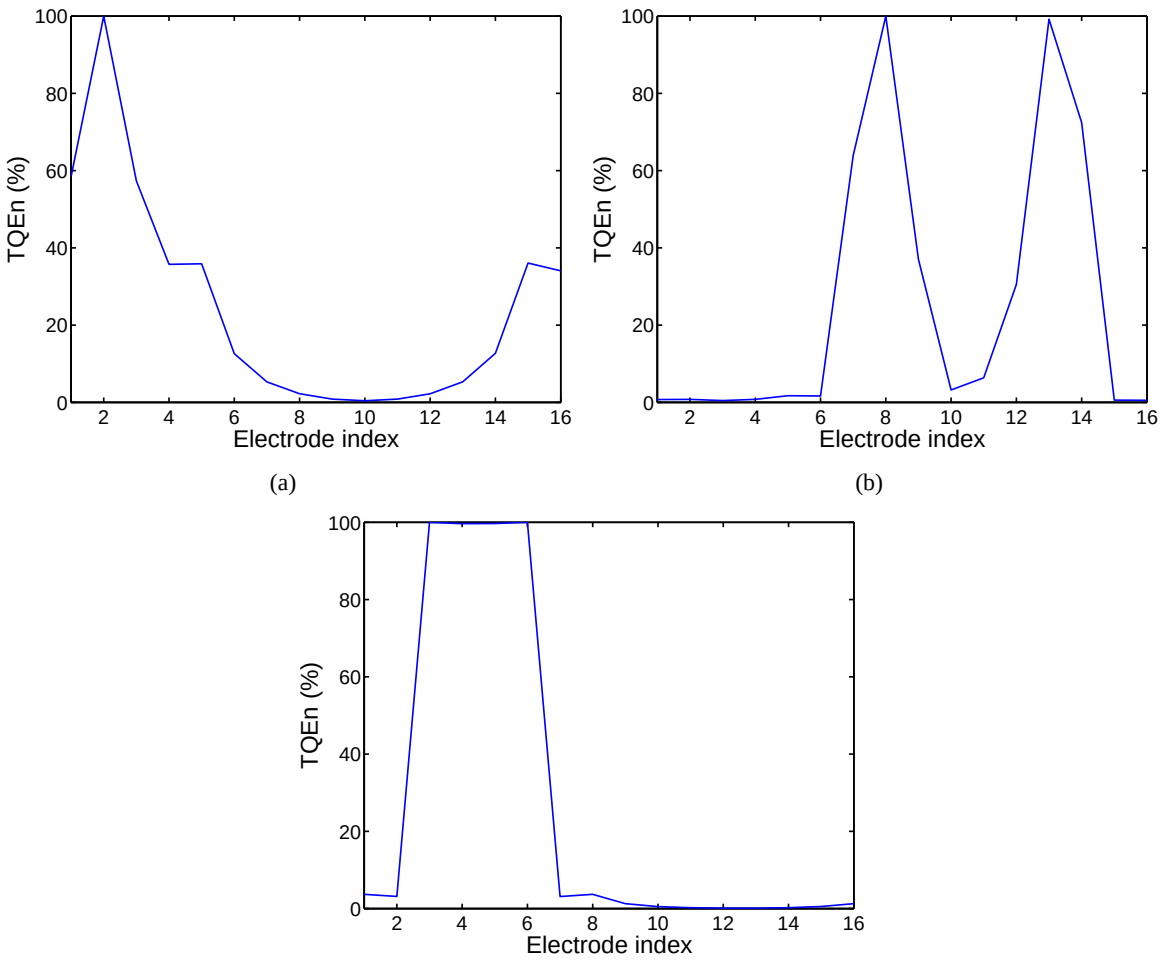

Fig. 6. Normalized total quadratic error (**TQEn**) in percentage (a) when electrode 2 is faulty, (b) when electrodes 8 and 13 are erroneous, and (c) when electrodes 4 and 5 are faulty.

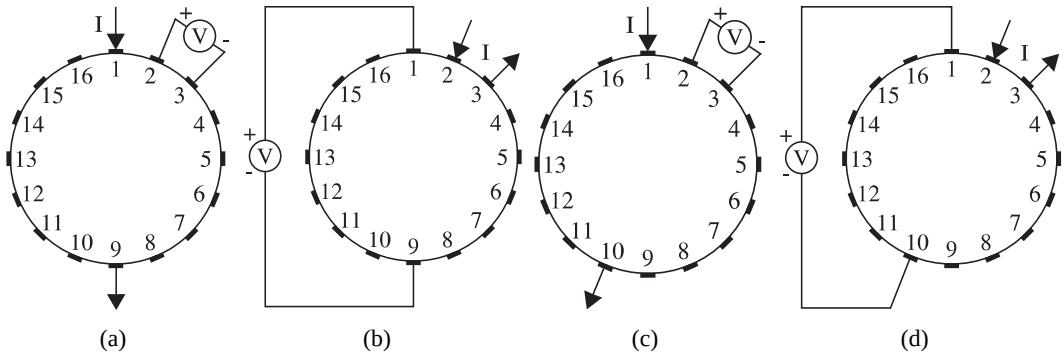

Fig. 7. Alternative acquisition protocols. (a) Opposite-drive adjacent-measurement. (b) Adjacent-drive opposite-measurement. (c) Pseudo-opposite-drive adjacent-measurement. (d) Adjacent-drive pseudo-opposite-measurement.

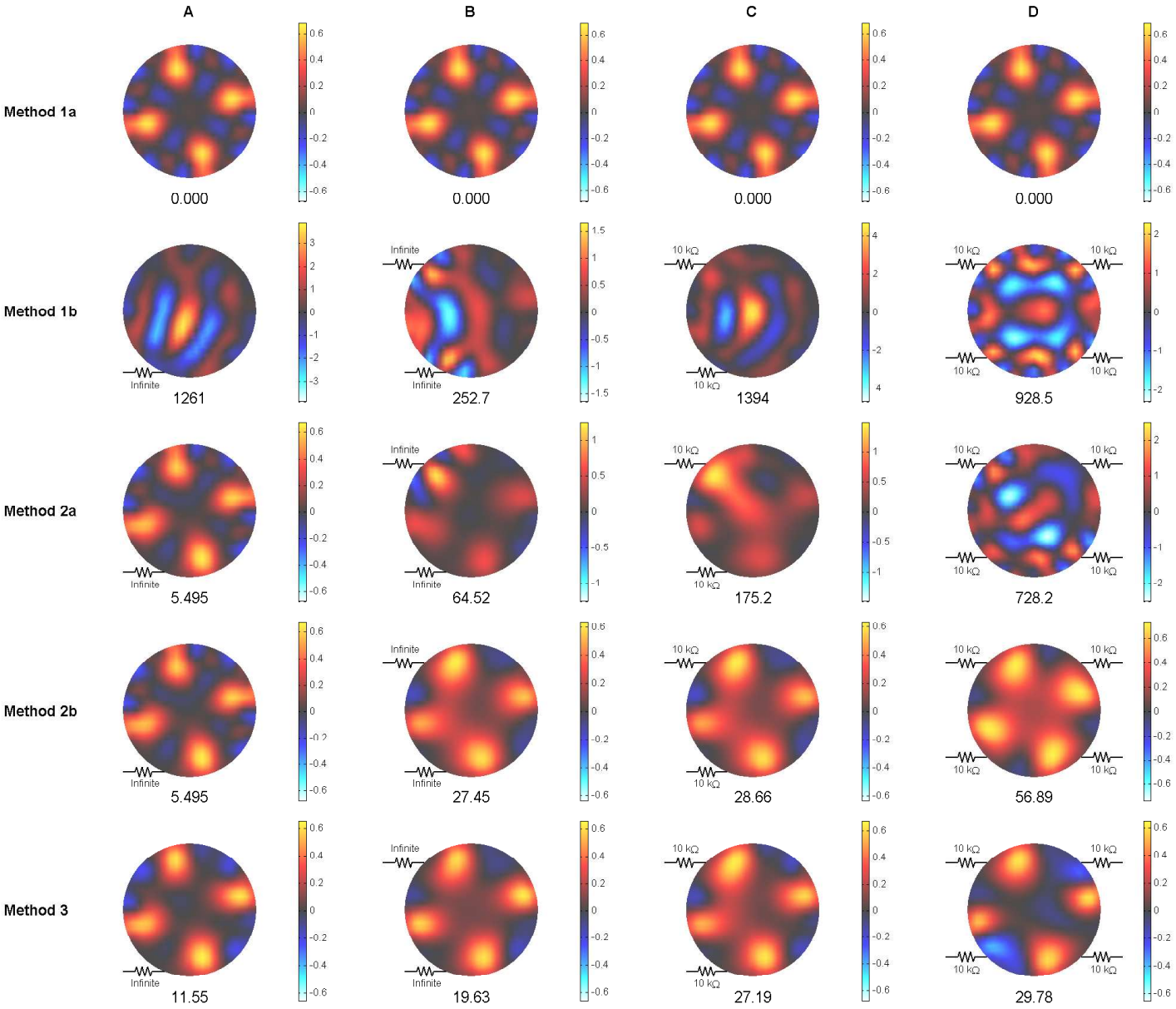

Fig. 8. Time difference images reconstructed from data acquired on a resistor mesh phantom with faulty electrodes. Columns A-D correspond to four different scenarios of partially and/or completely disconnected electrodes. Each line shows images reconstructed with the method indicated on the left. The first line, identified as *method 1a*, corresponds to images reconstructed with no disconnected electrode. Resistors indicate the location of the partially (10 kΩ) or completely (Infinite) disconnected electrodes. Warm colors are associated with a rise in conductivity while cool colors correspond to a decrease. The quadratic error (ϵ^2) is indicated below each image. A noise figure of 2 was used for all images [13].

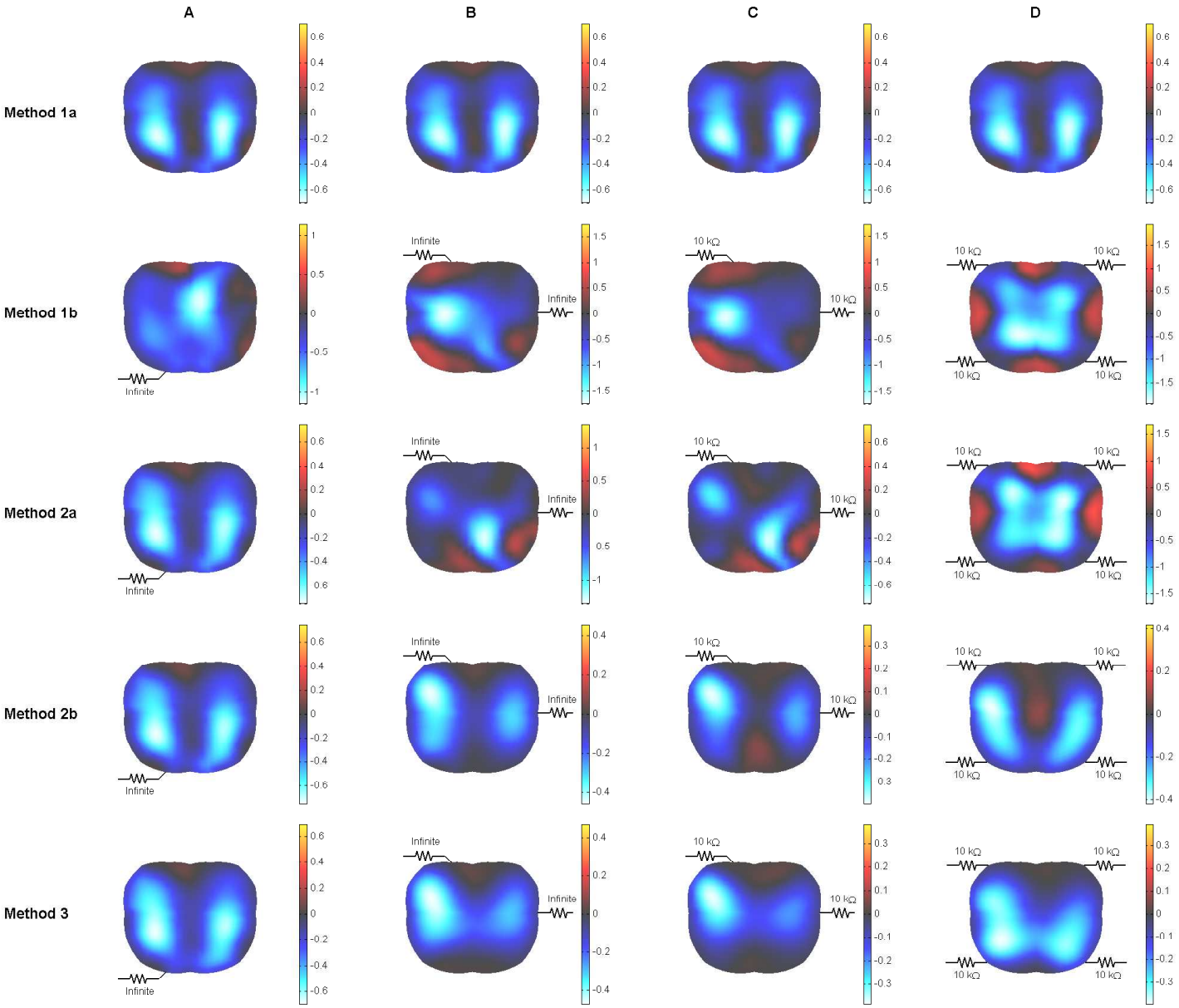

Fig. 9. Time difference images reconstructed from data acquired on a healthy male subject between full inspiration and expiration. Columns A-D correspond to four different scenarios of partially and/or completely disconnected electrodes. Each line shows images reconstructed with the method indicated on the left. The first line, identified as *method 1a*, corresponds to images reconstructed with no disconnected electrode. Resistors indicate the location of the partially (10 kΩ) or completely (Infinite) disconnected electrodes. Warm colors are associated with a rise in conductivity while cool colors correspond to a decrease. A noise figure of 0.75 was used for all images [13].

List of Tables

TABLE I
RESULTS FOR THE AUTOMATIC DETECTION ALGORITHM

Number of disconnected electrode(s)	Adjacent protocol		Opposite protocol		Pseudo-opposite protocol	
	Number of data sets	Number of correctly detected electrode(s)	Number of data sets	Number of correctly detected electrode(s)	Number of data sets	Number of correctly detected electrode(s)
None	9	0 (100%)	3	0 (100%)	3	0 (100%)
One	25	1 (100%)	4	1 (100%)	4	1 (100%)
Two	23	1 (4%)	4	1 (0%)	4	1 (0%)
		2 (96%)		2 (100%)		2 (100%)
Three	13	1 (61%)	—	—	—	—
		2 (31%)	—	—	—	—
		3 (8%)	—	—	—	—
Four	10	0 (70%)	—	—	—	—
		1 (30%)	—	—	—	—